Effect and mechanism of drum axial airflow regulation on threshed-material distribution in rapeseed harvesting

Chengpeng Li, Min Zhang*, Gang Wang, Tao Jiang, Jiaqi Zhao, Yanru Bi
(*Nanjing Institute of Agricultural Mechanization, Ministry of Agriculture and Rural Affairs, Nanjing 210014, China*)

Abstract: To address high cleaning losses caused by high impurity content and uneven distribution during rapeseed threshing, this study proposes a drum pneumatic-assisted threshing and separation method. Initially, by determining the suspension velocity characteristics of various threshed components, auxiliary blades were designed and integrated to construct a non-uniform gradient airflow field, generating a directional pneumatic transport effect. CFD simulations confirmed that this configuration induces a stable axial spiral airflow. Driven dynamically by this airflow, miscellaneous materials are guided to migrate orderly toward the rear of the concave screen, enabling active source-based regulation of the spatial-temporal flow behavior and component distribution. Multi-parameter correlation analysis indicated a significant negative correlation (coefficient = –0.88) between axial airflow and the average impurity ratio. Field experiments demonstrated that at a feed rate of 2.8 kg/s with auxiliary blades, the grain loss rate was reduced to 3.7%, compared with 6.3% without auxiliary blades, corresponding to a 41.3% reduction. This research demonstrates that axial airflow can effectively regulate threshed material at the source, providing a novel approach for high-efficiency and low-loss threshing and cleaning.
Keywords: rapeseed harvesting, pneumatic-assisted separation, threshed material distribution, grain loss rate
DOI: 10.25165/j.ijabe.20261903.10420

Citation: Li C P, Zhang M, Wang G, Jiang T, Zhao J Q, Bi Y R. Effect and mechanism of drum axial airflow regulation on threshed-material distribution in rapeseed harvesting. Int J Agric & Biol Eng, 2026; 19(3): 180–190.

1 Introduction

As a major global oilseed crop, rapeseed (*Brassica napus* L.) produces oil of high nutritional value, characterized by its richness in unsaturated fatty acids[1,2]. Furthermore, its byproduct, rapeseed cake, has demonstrated significant application potential in livestock feed and pharmaceuticals[3]. In major production regions such as Europe and North America, large-scale wheeled combine harvesters are widely employed. These machines are typically equipped with mature cleaning systems featuring multi-layer shaking plates and vibrating sieves, ensuring high-quality and efficient operations[4]. However, rapeseed cultivation in the Yangtze River Basin of China is primarily characterized by small-scale, scattered plots. Coupled with complex operating conditions such as frequent rainfall, high humidity, and heavy, sticky soil, large overseas machinery often faces challenges such as sinking and poor trafficability. Due to the constraints of field size and operating environments, small-scale tracked combine harvesters are predominantly used in China. Nevertheless, their compact structural design restricts the expansion of threshing drum dimensions and cleaning sieve areas. When processing high feeding rates, a dense and thick material layer tends to accumulate on the sieve surface, preventing grains from effectively penetrating the layer for separation. Consequently, grains are discharged from the machine along with the residue, resulting in excessively high loss rates. This issue has become a critical technical bottleneck hindering the high-efficiency and cost-effective development of the rapeseed industry in China.

To address the aforementioned challenges, extensive research has been conducted on the structural design and optimization of separation and cleaning systems in harvesting machinery. Regarding structural parameters and mechanism optimization, Liu et al.[5] developed a flexible discrete element model for rice plants using EDEM; by monitoring the drum's axial load, they systematically evaluated the impact of various rasp-bar configurations and threshing clearances on load uniformity. Liang et al.[6] focused on enhancing the airflow field within cleaning systems through optimized multi-duct devices; however, their approach offered limited intervention in the primary motion of materials within the threshing drum. Additionally, Dong et al.[7] revealed the regulatory role of sieve hole geometry on particle flow, while Fu et al.[8] established a contact mechanics model between grains and threshing components, demonstrating the distinct advantages of axial-flow drums in minimizing grain loss and damage. Yuan et al.[9] further utilized the discrete element method (DEM) to precisely characterize the properties of threshed components and successfully performed numerical simulations of the complex separation process within cylindrical sieves.

Regarding material migration mechanisms and spatial-temporal distribution characteristics, subsequent studies have further focused on the motion trajectories of threshed materials during the separation process. Ma et al.[10] quantitatively analyzed the dispersion and migration properties of agricultural particles, establishing a methodological foundation for motion law research. For flax and plot wheat, Dai et al.[11,12] developed gas-solid coupling simulation models to deeply analyze component migration patterns and the impact of improper operating parameters on material retention. Badretdinov et al.[13] mapped the physical flow field of the

Received date: 2026-01-30 **Accepted date:** 2026-05-28
Biographies: Chengpeng Li, PhD candidate, research interest: grain harvesting machinery, Email: licboom@163.com; **Gang Wang**, PhD, research interest: grain harvesting machinery, Email: wanggang05@caas.cn; **Tao Jiang**, PhD, research interest: grain harvesting machinery, Email: jiangtao01@caas.cn; **Jiaqi Zhao**, M.S. candidate, research interest: grain harvesting machinery, Email: 18041377879@163.com; **Yanru Bi**, MS candidate, research interest: grain harvesting machinery, Email: 82101232107@caas.cn.
***Corresponding author: Min Zhang**, Researcher and Doctoral Supervisor, research interest: grain harvesting machinery. Nanjing Institute of Agricultural Mechanization, Ministry of Agriculture and Rural Affairs, Nanjing 210014, China. Tel: +86-25-58619526, Email: zhm0912@126.com.

cleaning process in combine harvesters by measuring the airflow velocity at the sieve surface. Furthermore, Su et al.[14] and Li et al.[15] investigated the mechanisms by which whole-stalk feeding and novel sieve structures influence distribution uniformity and particle dispersion. Fu et al.[16] introduced a relative migration coefficient to evaluate the separation performance of corn mixtures on a new sieve surface, while Jin et al.[17] effectively improved the radial distribution uniformity of materials through an attitude angle fuzzy control strategy. Despite these advancements in optimizing cleaning system structures, most existing studies focus on downstream remedies within the cleaning unit, failing to address the excessive cleaning pressure caused by the initial threshing stage at its source. A critical bottleneck remains: the threshed output from the drum exhibits an excessively high impurity ratio and highly non-uniform spatial-temporal distribution, directly inducing congestion and grain losses in subsequent stages. Given the physical characteristics of rapeseed plants, such as their circumferential spiral motion within the threshing device and the low filling rate at the drum center[18], exploring the integration of a pneumatic-assisted separation system inside the drum holds significant research value for achieving source-based loss reduction.

Based on the aforementioned research strategy, this study developed a pneumatic-assisted threshing and separation device integrated within the threshing drum. By utilizing auxiliary blades mounted on the central shaft to generate a controlled airflow field, the device achieves active material regulation: aerodynamic forces and pressure differentials are leveraged to guide grains through the sieve efficiently, while simultaneously facilitating the migration of miscellaneous materials toward the rear discharge outlet. This mechanism enables the pre-emptive regulation of threshed component distribution during the threshing stage. Experiments were conducted to quantitatively analyze key indicators, including component proportions, distribution patterns, and grain loss rates, by comparing the performance of the auxiliary blades under various feed rates. The results aim to verify the feasibility of pneumatic-assisted technology in alleviating cleaning system pressure and minimizing harvesting losses, thereby providing a theoretical foundation for the design of compact rapeseed harvesting machinery.

2 Materials and methods

2.1 Working principle and mechanism analysis

2.1.1 Overall structure and working principle

The pneumatic-assisted threshing–separation device is designed to mitigate the non-uniform distribution of rapeseed threshed materials and the high impurity content by optimizing the airflow field. The prototype (Figure 1) retains the basic configuration of the 4LZ-6.0MEQ combine harvester, while two sets of auxiliary blades are innovatively integrated onto the main shaft of the threshing drum. The auxiliary blades were fabricated from high-strength steel and designed to withstand centrifugal and impact loads, ensuring sufficient structural strength and durability during operation. Each blade assembly adopts a four-blade symmetric arrangement with an installation angle of 25°. This angle was determined through preliminary experiments based on suspension velocity considerations, which indicated that 25° provides an optimal balance between axial thrust generation (within the effective airflow range for particle transport) and airflow stability. The rotational radius is 196 mm, and the axial spacing between the two blade assemblies is 590 mm, designed to generate a stable auxiliary separating airflow during operation. The axial spacing was determined based on the effective working length of the threshing drum, corresponding approximately to half of the effective drum length, thereby ensuring adequate coverage of the separation region while avoiding excessive overlap of adjacent disturbance zones and promoting uniform axial airflow regulation and particle transport. To quantitatively evaluate the operating performance of the device, a matrix-type sampling box was installed beneath the concave sieve. The sampling box, with overall dimensions of 1489 mm (L)× 745 mm (W)×150 mm (H), consists of 32 sub-boxes arranged in a 4×8 grid (4 columns×8 rows) to capture the spatial distribution of threshed materials. The longitudinal division into 8 sections (Rows 1-8) corresponds approximately to equal subdivisions of the effective working length of the threshing drum, enabling detailed characterization of axial material distribution. This matrix layout allows for zonal collection and accurate quantification of the threshed mixture, providing data support for analyzing material distribution patterns and optimizing system parameters.

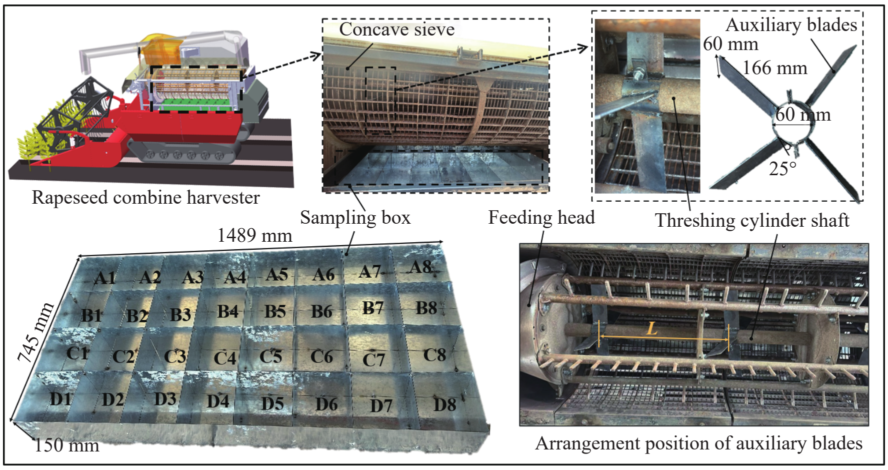

Figure 1 Schematic of the pneumatic-assisted threshing-separation device

As shown in Figure 2, the operating process of the device consists of three key stages: threshing–separation, sieving and falling-through, and distributed collection. During the threshing–separation stage, rapeseed plants are forced into the drum by the screw feeding header and are impacted and fragmented by the threshing elements. Two sets of rotating auxiliary blades establish a tailored airflow field within the threshing chamber, thereby improving the suspension state of the material, preventing material accumulation, and promoting the transport of lightweight impurities toward the straw outlet. During the sieving and falling-through stage, the airflow-induced disturbance disrupts the agglomerated structure of the material layer and accelerates the grain pass-through process. Owing to differences in aerodynamic characteristics among the components, the mixture follows distinct trajectories under the coupled action of airflow and gravity, achieving preliminary pneumatic-assisted separation. During the distributed collection stage, a matrix-type sampling box is used to capture the settled materials in different zones. By analyzing the spatial distribution and composition of the collected materials under various operating parameters, the separation performance of the pneumatic-assistance system can be quantitatively evaluated, providing data support for parameter optimization of the device.

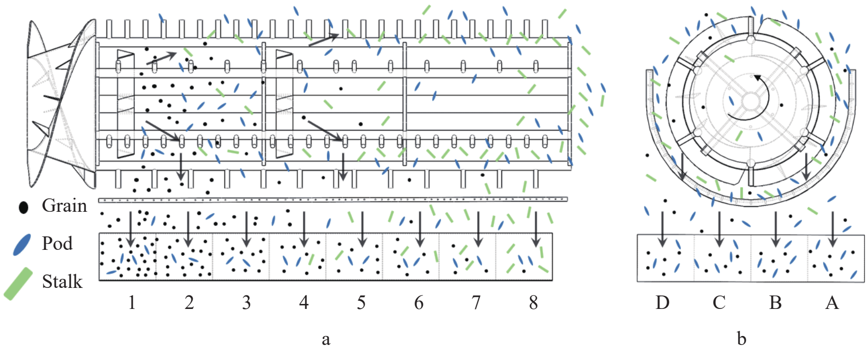

Figure 2 Working process of the pneumatic-assisted threshing–separation device

2.1.2 Effect of feed rate on the threshing and separation performance of the device

The screw feeding header of the pneumatic-assisted threshing-separation device adopts a dual-auger feeding mode. The design objective is to convey rapeseed plants steadily into the threshing drum while avoiding material congestion. A force analysis was conducted for a representative material particle on the auger blade during feeding (taking the feeding point O as an example). Gravity and the supporting force exerted by the feeding header on the material were neglected, as illustrated in Figure 3. Here, T denotes the normal thrust applied by the auger blade to the rapeseed material; it acts perpendicular to the blade-material contact surface and points downward, and the helix angle is α. F_f represents the friction force between the material and the auger blade; it is tangential to the contact surface and directed downward, with a friction angle β of 24°-35°[19]. The resultant force F is the vector sum of T and F_f. To ensure smooth feeding and prevent blockage, the conveying force generated by the auger blade should be greater than the axial resistance[20]. The corresponding relationship can be expressed as follows:

$$T\mathrm{Cos}\beta > F_f \sin\beta \tag{1}$$

$$F_f = T\tan\alpha \tag{2}$$

According to Equations (1) and (2), the criterion for the stable transport of material along the spiral feeding head is defined as $\alpha+\beta<90°$. The term $F\cos(\alpha+\beta)$ represents the axial component of the resultant force F. Since a greater axial force component correlates with higher material transport efficiency, $\cos(\alpha+\beta)$ is defined as the material transport efficiency coefficient. The spiral angle α and the length l_1 of the spiral feeding head are calculated using the following equations[21]:

$$\alpha = \arctan\left(\frac{KS}{\pi D}\right) \tag{3}$$

$$l_1 = SN \tag{4}$$

where, S is the helix pitch (mm); D is the outer diameter of the auger, mm; K is the number of screw starts (set to 2); and N is the effective number of turns of the screw flight (set to 0.5).

The spiral feeding head features a frustum structure (truncated cone). By combining Equation (3) and Equation (4), the design parameters were determined as follows: the pitch S was 490 mm, the length l_1 was 245 mm, the outer diameter D was 620 mm, and the front and rear diameters (d_1 and d_2) were 325 mm and 490 mm, respectively. Consequently, the spiral angle α was calculated to be 26.8°, which satisfies the smooth feeding criteria, confirming the rationality of the design. Under the premise of a constant spiral angle α, the mass feed rate (Q) serves as the core quantitative indicator for aligning the feeding head performance with harvesting efficiency. A reasonable feed rate is essential for enhancing the quality of rapeseed harvesting. According to previous studies[22,23], the formula for calculating the mass feed rate Q is derived as:

$$Q = \rho\varphi\frac{\pi(D^2 - d_m^2)}{4}nS\eta\tau \tag{5}$$

$$\eta = \cos(\theta + \alpha) \tag{6}$$

where, ρ is the average material density (200 kg/m³); φ is the volume filling coefficient (0.08); d_m is the mean shaft diameter, calculated as $(d_1+d_2)/2$; n is the rotational speed (600 r/min); η is the conveying efficiency; and τ is the correction coefficient, ranging from 0.4 to 0.45.

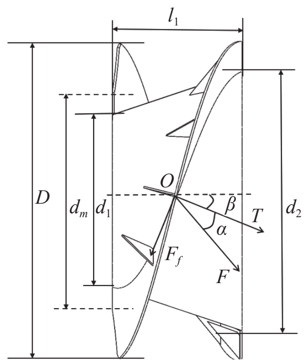

Figure 3 Force analysis and structural design of the screw feeding header

Based on Equation (5) and Equation (6), the theoretical mass feed rate of the spiral feeding head was calculated to be 2.7-5.2 kg/s. Consequently, representative feed rates of 2.8 kg/s and

4.2 kg/s were selected for verification in the field trials.

2.1.3 Mechanical analysis of silique impact and grain penetration within the rapeseed threshing drum

To investigate the kinetic behavior of rapeseed material within the threshing drum, a nail-tooth collision model was established based on impact mechanics. The threshing teeth and auxiliary blades rotate counter-clockwise around the drum axis at an angular velocity ω. A Cartesian coordinate system was established with the rotation center O of the threshing drum as the origin. The Y-axis (normal direction) is defined along the radial line pointing toward the concave, while the X-axis (tangential direction) is perpendicular to the Y-axis along the direction of motion. As illustrated in Figure 4a, the silique is subjected to several forces during the impact: Impact force (F): Applied by the threshing tooth, forming an angle θ_1 with the direction of gravity (G). Aerodynamic thrust (F_d): Generated by the induced airflow, with its direction forming an angle θ_2 with the normal direction (Y-axis). Centrifugal force (F_c): Resulting from the high-speed rotation of the drum. Support force (F_n) and Friction (F_f): Arising from the interaction and compression between the nail-tooth and the material layer. Based on kinematic principles, the motion of grains adjacent to the concave screen was analyzed. Similarly, a tangential-normal coordinate system was established with the drum center O as the origin (Figure 4b). During the penetration process, the forces acting on the grain include: Centrifugal force (F_{c2}) and Gravity (G_2), where θ_4 represents the angle between gravity and the normal direction. Aerodynamic thrust (F_d): Generated by the auxiliary blades, forming an angle θ_3 with the tangential direction (X-axis). Support force (F_{n2}) and Friction (F_{f2}): Exerted by the concave screen surface.

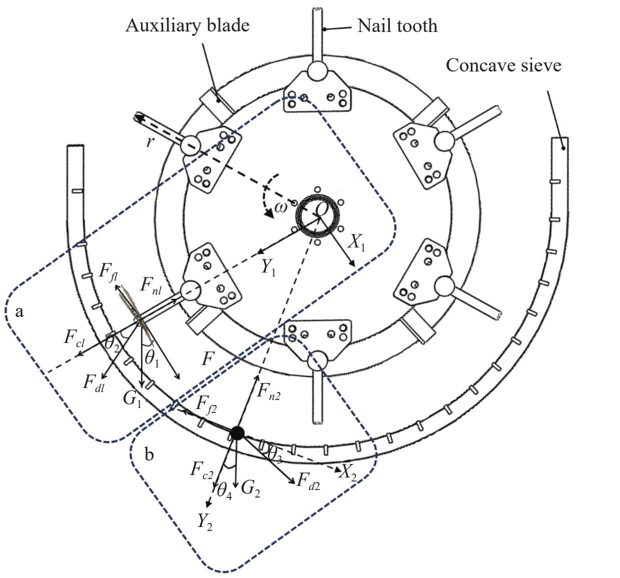

Figure 4 Mechanical models of rapeseed material during threshing and separation

According to the silique-tooth collision model, the aerodynamic drag force (F_d) generated by the airflow is calculated as follows[24]:

$$F_d = \frac{1}{2} C_d \rho_{air} A v^2 \tag{7}$$

where, C_d is the drag coefficient, which is dependent on the silique shape and the Reynolds number; ρ_{air} is the air density, kg/m³; A is the projected area (frontal area) of the silique, m²; v is the airflow velocity, m/s.

The centrifugal force is calculated as follows:

$$F_c = m\omega^2 r \tag{8}$$

where, m is the mass of the silique, kg; r is the rotation radius (the distance from the impact point to the drum axis), m.

Based on Newton's second law, the governing equations of motion for the silique in the tangential and normal directions are derived as follows:

$$\begin{cases} mr\dfrac{\mathrm{d}\omega}{\mathrm{d}t} = F + F_{d1}\sin\theta_2 + G_1\cos\theta_1 - F_{f1} \\ m\dfrac{\mathrm{d}v}{\mathrm{d}t} = F_{c1} + F_{d1}\cos\theta_2 + G_1\sin\theta_1 - F_{n1} \end{cases} \tag{9}$$

The results from Equation (9) demonstrate that the helical forward motion of the silique is formed by the coupling of aerodynamic disturbance and tangential circular motion, while the radial force determines its contact state with the drum wall. Under constant conditions of drum rotational speed, threshing tooth geometry, and grain moisture content, the helical motion characteristics of the silique are directly governed by the airflow velocity. In mechanized rapeseed harvesting, the grain penetration efficiency is influenced by multi-force coupling effects. Elucidating the penetration mechanism from a mechanical perspective is of great significance for enhancing harvesting performance. The dimensions of the concave apertures in this system are 22 mm×50 mm (length×width). According to previous research[25], the average triaxial dimensions (length×width×height) of rapeseed grains are 2.11 mm×1.95 mm×1.85 mm, which strictly satisfy the geometric criteria for grain penetration[26].

To ensure successful grain penetration through the concave screen, the resultant forces in both the tangential and normal directions must be greater than zero[27]. This criterion can be expressed as:

$$\begin{cases} F_{d2}\cos\theta_3 + G_2\sin\theta_4 \geq F_{f2} \\ F_{d2}\sin\theta_3 + G_2\cos\theta_4 + F_{c2} \geq F_{n2} \end{cases} \tag{10}$$

As indicated by Equation (10), the aerodynamic force facilitates the penetration motion of grains, effectively shortening their residence time within the threshing drum and consequently reducing entrainment loss. An optimal range of airflow velocity is essential for achieving a balance between the grain penetration rate and the impurity filtration quality. While elevated airflow velocity enhances penetration efficiency, excessive speeds may trigger the penetration of miscellaneous materials and increase axial grain entrainment loss. To determine the optimal aerodynamic parameters, the following sections combine terminal velocity measurements of the materials with Computational Fluid Dynamics (CFD) simulations of the auxiliary blades. This approach provides a theoretical foundation for the design of pneumatic-assisted devices through the precise regulation of the airflow gradient.

2.2 Simulation analysis of material suspension velocity and airflow field

2.2.1 Measurement of suspension velocity for threshed components

To clarify the aerodynamic properties of various rapeseed components, the suspension velocities of threshed materials were determined using a specialized test bench (Figure 5). The apparatus primarily consists of a material mesh (20-mesh nylon), a feeding inlet, a conical observation tube, upper and lower steady-flow tubes, an anemometer, a fan, a variable frequency drive (VFD), a frame, and connecting assemblies. During the experiment, each component was fed onto the mesh in the lower steady-flow tube. The fan was initiated at an air velocity of 0.5 m/s, which was then incrementally increased by 0.1 m/s using the VFD. After allowing the airflow to stabilize for 20 s, the motion of the material was observed for 5 s. The air velocities in the steady-flow tubes and the suspension height within the conical tube were recorded when the material reached a state of stable suspension—characterized by neither sinking nor escaping, but merely oscillating slightly within the airflow. The suspension velocity was subsequently calculated according to Equation (11)[28]. Each test was repeated five times per component. The experimental results for the suspension velocities and airflow field measurements are summarized in Table 1.

$$v_f = \bar{v}\left(\frac{R}{R+H\tan\gamma}\right)^2 \tag{11}$$

where, v_f is the suspension velocity of the tested material (m/s), calculated as the mean air velocity of the upper and lower steady-flow tubes; R is the inner radius of the conical observation tube (200 mm); H is the suspension height of the material within the conical tube (0-1000 mm); and γ is the inclination angle of the conical observation tube (4°).

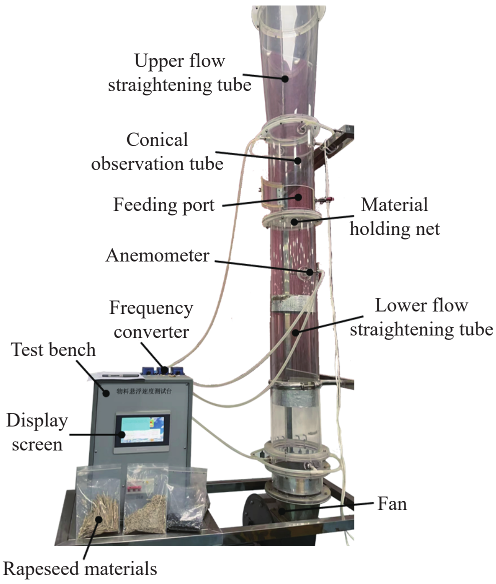

Figure 5 Suspension velocity measurement apparatus

Table 1 Suspension velocity measurements of various threshed components

Threshed components	Suspension velocity range/m·s^{-1}
Grains	6.8 - 11.2
Pods	2.4 - 3.2
Stalks	5.3 - 12.2
Miscellaneous	1.1 - 3.2

Note: Ambient temperature 25°C, relative humidity 50%.

2.2.2 CFD simulation setup

In this study, the computational fluid dynamics (CFD) software ANSYS Fluent 2024 R1 was employed to numerically solve the internal flow field of the pneumatic-assisted device. Initially, a three-dimensional geometric model of the pneumatic-assisted threshing and separation device was established using SolidWorks 2025. Subsequently, mesh generation was performed within the Mesh module of ANSYS Workbench 2024 R1. Given the complexity of the computational domain, a tetrahedral unstructured mesh was adopted for discretization. The mesh exhibited an average orthogonal quality of 0.79, which satisfies the requirements for numerical stability and computational accuracy, as illustrated in Figure 6.

Regarding the solver settings, the Re-Normalization Group (RNG) k-ε turbulence model was selected due to its superior capability in resolving flow fields with high strain rates, strong swirling motion, and pronounced streamline curvature. Given that the internal flow is characterized by intense rotation and gas–solid coupling, the regime can be considered fully turbulent; thus, model selection is governed by flow characteristics rather than explicit Reynolds number evaluation. The Sliding Mesh technique was employed to simulate the rotational motion of the auxiliary blades at a speed of 600 r/min. The boundary conditions were defined as follows: both the feeding inlet and the material outlet were set as Pressure Boundaries (Pressure inlet/outlet), with the relative pressure set to standard atmospheric pressure (0 Pa gauge pressure). The housing surface was designated as a Stationary Wall. The convergence criteria for the solution were set to a residual value of less than 1×10^{-3}. The time step for the gas-phase calculation was defined as 1×10^{-3} s, and the simulation was continued until the flow field reached a dynamically stable state.

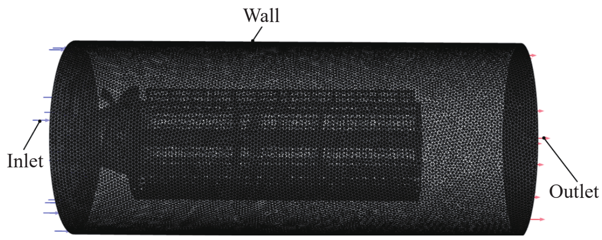

Figure 6 Mesh generation of the computational domain

2.3 Field experiment on the pneumatic-assisted threshing and separation device

As shown in Figure 7a, to evaluate the field performance and separation effectiveness of the pneumatic-assisted threshing and separation device, field trials were conducted in June 2025 at the rapeseed cultivation base in Dafeng District, Yancheng City, Jiangsu Province, China (33°12′N, 120°28′E). The variety used for testing was "Fengyou 737", which was at the full maturity stage, satisfying the requirements for threshing and separation experiments. The measured agronomic traits of the rapeseed in the experimental plots were as follows: the average plant height was 153.9 cm, the branching height was 77.6 cm, and the number of effective branches per plant was 3.95. The number of effective siliques per plant was 145.2, with an average of 19.6 seeds per silique. Additionally, the 1000-grain weight was 3.72 g, and the moisture content ranged from 12.62% to 15.65%. The detailed experimental design is listed in Table 2.

Taking Scheme 3 as an example, the operational procedure was conducted as follows: First, two sets of auxiliary blades and the material collection boxes were installed in their designated positions on the rapeseed combine harvester. Subsequently, the rapeseed plants were precisely weighed using an electronic balance and fed uniformly into the machine manually. Throughout the experiment, the rotational speed of the threshing drum was maintained constant at 600 r/min. Upon completion of the threshing operation, the collection boxes were retrieved from the rear of the machine, and a portable vacuum device was employed to collect all materials within the boxes. Finally, the recovered materials were classified using standard test sieves with various apertures to separate the mixture into grains, pods, stalks, and miscellaneous materials, which were then bagged individually. The detailed operational workflow is illustrated in Figures 7c and 7d.

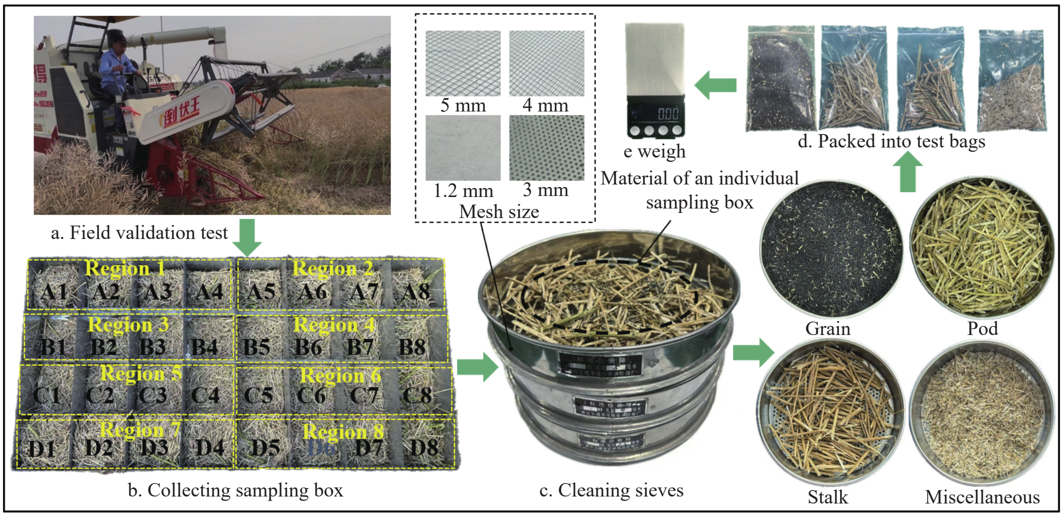

Figure 7 Experimental procedure

Table 2 Experimental schemes

Scheme	Parameter combination
1	Feeding rate: 2.8 kg/s, without auxiliary blades
2	Feeding rate: 4.2 kg/s, without auxiliary blades
3	Feeding rate: 2.8 kg/s, with auxiliary blades
4	Feeding rate: 4.2 kg/s, with auxiliary blades

All categorized materials after sieving were weighed using an electronic balance, as illustrated in Figure 7e. The experimental data were recorded and labeled according to the spatial coordinates of the collection boxes, denoted as M_{Gmn}, M_{Pmn}, M_{Smn}, and M_{Mmn}, where the subscripts G, P, S, and M represent grains, pods, stalks, and miscellaneous materials, respectively. The indices m and n designate the column and row numbers of the collection boxes within the sampling matrix. Based on the spatial mass distribution data of these components, the regulatory effect of the pneumatic-assisted separation system on the threshed output was systematically evaluated. The mass proportion of each component, grain loss rate, and Coefficient of Variation of distribution uniformity were selected as the primary evaluation indicators. The calculation methods are defined as follows:

(1) Mass proportions of threshed components

The mass proportions of threshed components are employed to characterize the spatial distribution characteristics of various materials passing through the concave screen into the collection boxes under diverse operational conditions. This evaluation primarily encompasses the individual box proportion, average proportion, and column-wise proportion. Taking collection box A1 (the box at the first column and first row) as an example, the mass proportions of grains, pods, stalks, and miscellaneous materials within the box are calculated using the following formulas:

$$\begin{cases} W_{GA1} = \dfrac{M_{GA1}}{M_{GA1}+M_{PA1}+M_{SA1}+M_{MA1}} \times 100\% \\ W_{PA1} = \dfrac{M_{PA1}}{M_{GA1}+M_{PA1}+M_{SA1}+M_{MA1}} \times 100\% \\ W_{SA1} = \dfrac{M_{SA1}}{M_{GA1}+M_{PA1}+M_{SA1}+M_{MA1}} \times 100\% \\ W_{MA1} = \dfrac{M_{MA1}}{M_{GA1}+M_{PA1}+M_{SA1}+M_{MA1}} \times 100\% \end{cases} \tag{12}$$

The average mass proportions of grains, pods, stalks, and miscellaneous materials across the sampling matrix are calculated as follows:

$$\begin{cases} \bar{W}_{GA1} = \dfrac{W_{GA1}+\ldots+W_{GD8}}{32} \times 100\% \\ \bar{W}_{PA1} = \dfrac{W_{PA1}+\ldots+W_{PD8}}{32} \times 100\% \\ \bar{W}_{SA1} = \dfrac{W_{SA1}+\ldots+W_{SD8}}{32} \times 100\% \\ \bar{W}_{MA1} = \dfrac{W_{MA1}+\ldots+W_{MD8}}{32} \times 100\% \end{cases} \tag{13}$$

The column-wise mass proportions of grains, pods, stalks, and miscellaneous materials (representing the distribution proportions of each component along the axial direction of the threshing drum) are calculated as in the following equation:

$$\begin{cases} \omega_{GA1} = \dfrac{M_{GA1}}{M_{GA1}+\ldots+M_{GA8}} \\ \omega_{PA1} = \dfrac{M_{PA1}}{M_{PA1}+\ldots+M_{PA8}} \\ \omega_{SA1} = \dfrac{M_{SA1}}{M_{SA1}+\ldots+M_{SA8}} \\ \omega_{MA1} = \dfrac{M_{MA1}}{M_{MA1}+\ldots+M_{MA8}} \end{cases} \tag{14}$$

(2) Coefficient of Variation (CV) for distribution uniformity

To quantify the impact of the pneumatic-assisted threshing and separation device on the axial and radial distribution of threshed materials, the collection area was divided into eight regions, as shown in Figure 7b. The formula for calculating the coefficient of variation of the impurity mass uniformity is as in the following equation:

$$CV = \frac{\bar{X}}{\sqrt{\dfrac{\sum_{Region=1}^{8}(x_{Region}-\bar{X})}{8}}} \times 100\% \tag{15}$$

where, $\bar{X}$ is the mean mass of the threshed impurities across the eight regions, g; x_{region} is the mass of the threshed impurities in the region, g.

(3) Grain loss rate

During the experiments, a manual sampling method was employed to collect the mixtures discharged from the impurity outlet of the threshing drum and the cleaning outlet. After the sieving process, the mass of the lost grains was measured and recorded as M_1. The total mass of grains recovered from all collection boxes was recorded as M_2. The grain loss rate, denoted as

Q, was calculated using the following equation:

$$Q = \frac{M_1}{M_1 + M_2} \times 100\% \quad (16)$$

Based on the aforementioned experimental conditions, four sets of field comparison trials were sequentially conducted according to the predefined schemes.

3 Results and discussion

3.1 Analysis of airflow field simulation results

The internal flow field simulation results systematically revealed the spatiotemporal evolution patterns and steady-state characteristics of the pneumatic-assisted device (Figure 8). As illustrated in Figure 8a, the flow field underwent a complete transition from transient disturbance to steady-state evolution. During the initial startup phase (0-0.3 s), the high-speed rotation of the auxiliary blades rapidly induced near-field air fluctuations. With the continuous transfer and accumulation of momentum within the chamber, the flow field stabilized by 0.7 s, forming a distinct axial spiral airflow. This confirms the device's superior capacity for flow-field induction and power transmission. The velocity contours in Figure 8b further reveal a prominent alternating velocity gradient field within the threshing space, with local air velocities in the core working area maintained at 7-11 m/s. In conjunction with the suspension velocities of the components measured in Section 2.2.1, this velocity range effectively targets lightweight components, overcoming the physical interlocking forces within the rapeseed mixture. Although the core airflow velocity (7-11 m/s) is lower than the suspension velocity of stalks (12.2 m/s), axial transport is primarily driven by the combined effects of aerodynamic drag, blade-induced disturbance, and particle interactions. Under these conditions, sub-suspension airflow can still promote sliding, rolling, and intermittent lifting of stalk particles, thereby enabling effective axial migration. By inducing a fluidization and loosening effect through aerodynamic loads, the airflow drives impurities, such as pods, to migrate orderly toward the rear of the concave screen. This transport and penetration action significantly reduces material retention, optimizes spatial distribution, and alleviates the operational load on the cleaning sieve at the source. Consequently, entrainment losses caused by material accumulation are effectively curtailed, markedly enhancing the overall threshing and separation efficiency.

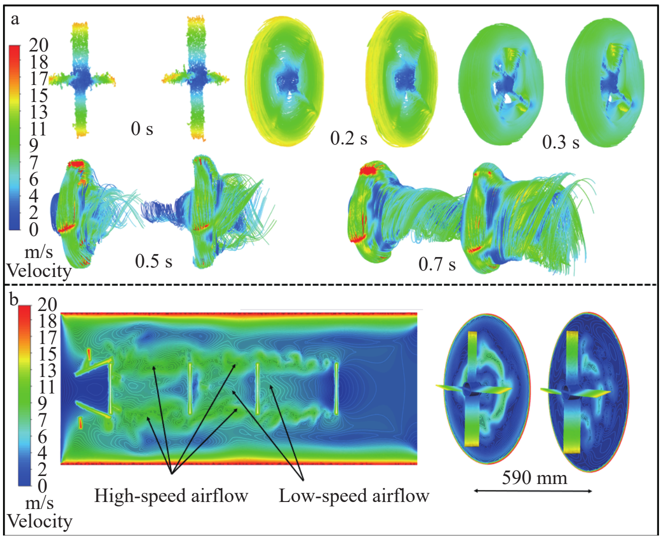

Figure 8 Formation characteristics and velocity contours of the internal flow field in the pneumatic-assisted device

3.2 Analysis of field experimental results

3.2.1 Analysis of threshed material penetration distribution characteristics

(1) Analysis of component proportions in small collection boxes

Based on the aforementioned experimental procedure and Equation (12), distribution maps for threshed material across 32 small collection boxes were generated for each scheme. As illustrated in Figure 9, the grain proportion exhibited a declining trend along the drum's axial direction. Conversely, the pod proportion followed a parabolic trend (initially increasing and then decreasing), while the stalk proportion increased progressively. The proportion of miscellaneous materials remained relatively stable. The underlying mechanism for these trends is as follows: in the front section of the drum, pods are rapidly crushed by the impact of the threshing teeth, causing grains to detach and penetrate the concave screen quickly. Initially, the penetration rate of pods is low; however, as the threshing process intensifies and pods are further fragmented, their penetration peaks in the middle section. Stalks, characterized by their structural rigidity and lengths typically exceeding the concave screen apertures, tend to migrate and accumulate toward the rear. Under identical feeding rates, the peak pod proportions in Scheme 1 were located at A5, B7, C5, and D6.

In contrast, in Scheme 3, these peaks shifted to A8, 6, C7, and D7, indicating a significant rearward migration along the drum. This suggests that the auxiliary airflow successfully altered the motion trajectories of the pods; the aerodynamic thrust reduced the penetration probability of lightweight pods, forcing them toward the rear of the drum. Furthermore, a comparison between Scheme 2 (peaks at A8, B7, C8, D8) and Scheme 4 (peaks at A6, B6, C7, D7) reveals that the rearward displacement of the pod peak in Scheme 2 was substantially more pronounced than that in Scheme 4.

(2) Analysis of average component proportions

Based on Equation (13), the average proportions of each component under the four experimental schemes were calculated, with the results illustrated in Figure 10. The analysis reveals significant differences in material composition across the schemes: from Scheme 1 to Scheme 4, the average grain proportion exhibited a progressive increase, while the proportion of impurities in the threshed material decreased systematically. Specifically, in Scheme 1, the grain proportion was only 38.5%, accompanied by high impurity content (41.9% pods, 15.2% stalks, and 4.4% miscellaneous). In contrast, the grain proportion in Scheme 4 increased to 50.3%, with all impurity categories showing a marked decline; specifically, pods, stalks, and miscellaneous dropped to 35.6%, 10.5%, and 3.6%, respectively. Data comparison demonstrates that compared to Scheme 1, Scheme 4 achieved an 11.8 percentage point increase in average grain proportion, while the proportions of pods, stalks, and miscellaneous were reduced by 6.3, 4.7, and 0.8 percentage points, respectively. These significant changes fully validate the effectiveness of the pneumatic-assisted threshing and separation device in optimizing threshed component distribution and enhancing separation performance.

(3) Analysis of column-wise distribution proportions

Based on Equation (14), the column-wise distribution proportions of the threshed components for the four experimental schemes are illustrated in Figure 11. In all schemes, grains were primarily concentrated in the front section of the drum (Rows 1–4), with their proportions exhibiting a decreasing trend along the axial direction. The mean grain proportions in the front section followed the order: Scheme 4 (90.8%) > Scheme 2 (88.7%) > Scheme 3 (88.1%) > Scheme 1 (87.2%). These results indicate that grains have a limited axial migration distance, and the introduction of auxiliary blades exerted no significant influence on their distribution patterns. Conversely, the stalk proportion followed an increasing trend along the axial direction, with concentrations mainly in the rear section of the drum (Rows 6-8). The mean stalk proportions in the rear section were ranked as follows: Scheme 4 (66.6%) > Scheme 1 (60.5%) > Scheme 2 (55.8%) > Scheme 3 (54.3%). It can be observed that stalks underwent a slight axial displacement. This is primarily attributed to the matching between the stalk suspension velocity and the auxiliary airflow field, which promoted the rearward transport of lightweight stalks during the separation process.

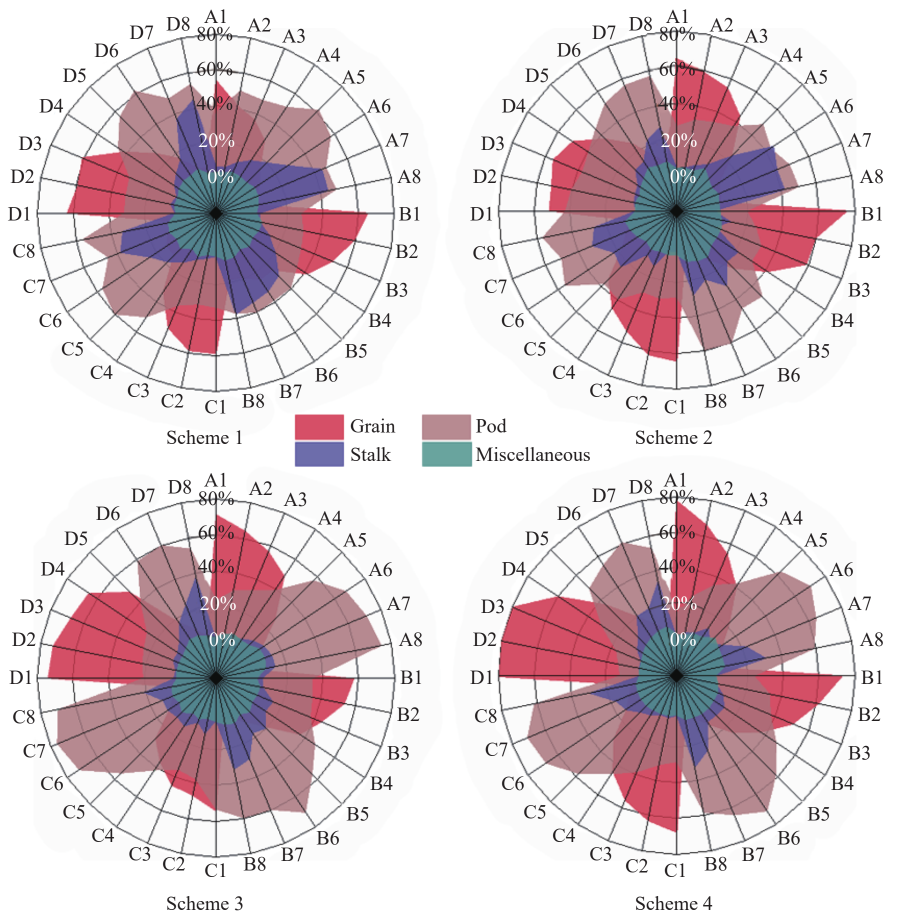

Figure 9 Mass proportions of threshed material after penetration for the four schemes

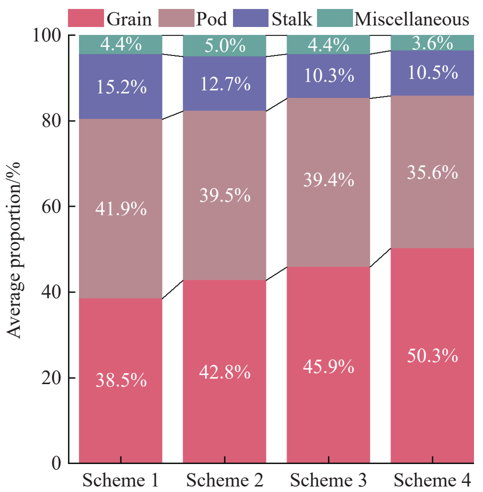

Figure 10 Average proportions of threshed materials for the four schemes

In Schemes 1 and 3, where auxiliary blades were not installed, the pods exhibited a distribution pattern characterized by a "high concentration at the front and low at the rear" (with higher proportions in Rows 1-4). Conversely, in the schemes incorporating the airflow field, the mean proportion of pods in Rows 1-4 decreased (from 55.3% in Scheme 1 to 45.4% in Scheme 4), while the proportions in Rows 5–8 increased correspondingly. This indicates that the aerodynamic thrust generated by the pneumatic-assisted device successfully altered the motion trajectories of the pods, effectively mitigating the accumulation phenomenon in the front section. Furthermore, the increase in feeding rate was observed to exert a regulatory effect on the distribution. Regarding the distribution of miscellaneous materials, the proportions in the front section were higher than those in the rear section under the no-blade conditions (Schemes 1 and 3). Upon the introduction of auxiliary blades, the miscellaneous materials gradually migrated toward the rear section, with the mean proportion in the front section (Rows 1-4) decreasing to a minimum of 48.8% in Scheme 4. In conclusion, the installation of auxiliary blades, combined with an appropriate feeding rate, can significantly optimize the spatial distribution of threshed materials, effectively reducing the accumulation of pods, miscellaneous materials, and lightweight stalks in the front section of the drum.

3.2.2 Analysis of distribution uniformity *CV* and grain loss rate

Based on Equations (15) and (16), the Coefficient of Variation (*CV*) for distribution uniformity and the grain loss rate for each scheme were calculated, as illustrated in Figure 12. Under identical feeding rate conditions, the pneumatic-assisted threshing and separation device significantly enhanced the material distribution and reduced grain losses. Taking the feed rate of 2.8 kg/s as an example, Scheme 3 showed a reduction in the distribution *CV* of 2.7 percentage points and a decrease in the grain loss rate of 1.1 percentage points compared to Scheme 1. When the feed rate was increased to 4.2 kg/s, Scheme 4 exhibited a 5.7 percentage point reduction in the *CV* and a 2.6 percentage point decrease in the loss rate relative to Scheme 1. These results indicate that the introduction of the pneumatic-assisted device leads to a more uniform material distribution within the drum, thereby ameliorating grain loss. The mechanism underlying this improvement is the continuous and uniform aerodynamic disturbance generated by the front and rear auxiliary blades within the drum. This disturbance facilitates the separation and discharge of miscellaneous materials, such as pods and chaff, which in turn reduces the entrapment and remixing of grains within the impurity layer. Furthermore, the airflow promotes the smooth sedimentation of grains and mitigates the risk of sieve clogging, optimizing the penetration process. Recent literature [29] achieved a reduction in cleaning loss rate to 3.1% through multi-parameter system optimization. While the grain loss rate of 3.7% in Scheme 4 of this study is slightly higher, our approach offers distinct advantages, including a novel and simplified structure, lower space requirements, and the absence of a need for an external power source.

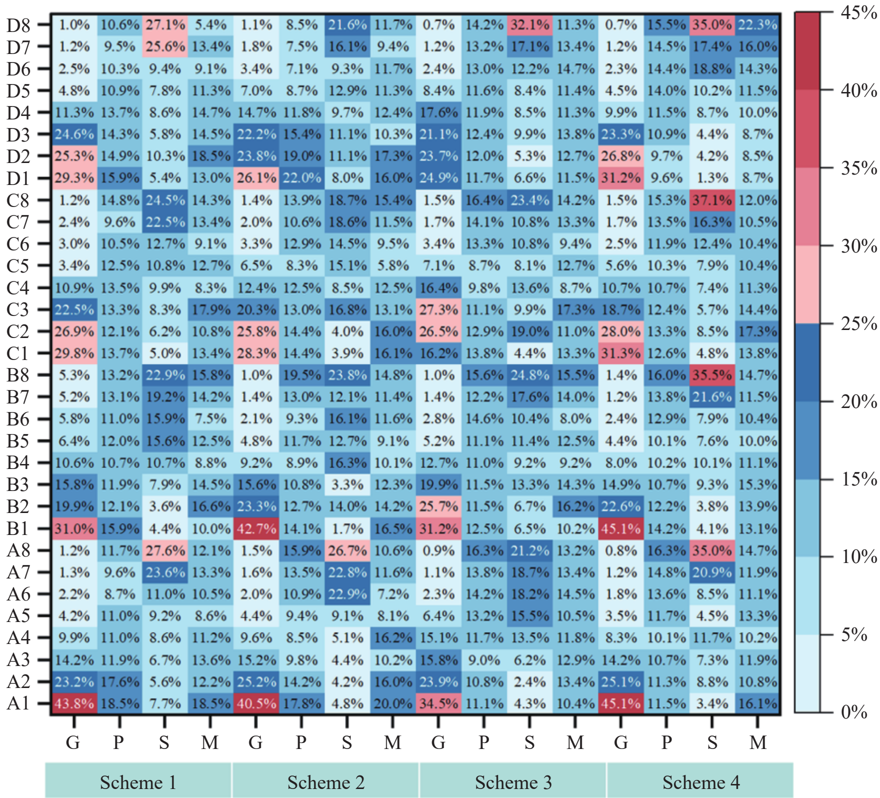

Note: G, P, S, and M represent grains, pods, stalks, and miscellaneous

Figure 11 Column-wise distribution proportions of various threshed components for the four experimental schemes

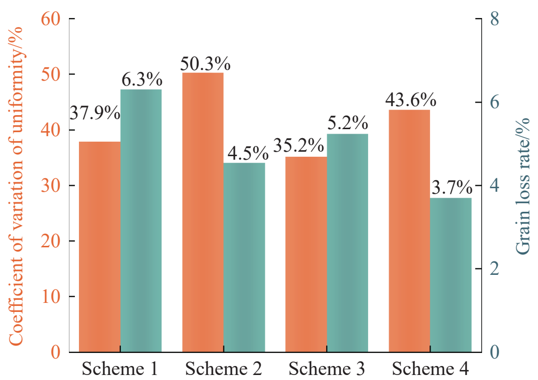

Figure 12 Grain loss rates and distribution uniformity *CV*s for the four experimental schemes

3.2.3 Correlation analysis between parameter combinations and evaluation indicators under different schemes

To investigate the effects of different schemes on harvesting performance, a correlation analysis was conducted between the parameter combinations and evaluation indicators. Pearson correlation analysis was performed using the Mixed method. The correlation analysis was performed based on the overall mean values of the four experimental schemes, enabling an evaluation of the global relationships between variables while reducing the influence of local spatial variability. As illustrated in Figure 13, a strong negative correlation (r = –0.88) was observed between the installation of auxiliary blades and the average impurity ratio in the threshed material, indicating that the pneumatic assistance effectively reduces the impurity content. The feeding rate exhibited a strong positive correlation with the distribution uniformity *CV* (r = 0.90), suggesting that the material distribution characteristics are highly sensitive to the feeding rate, with the distribution being optimized at 4.2 kg/s. Furthermore, a strong negative correlation was found between the feeding rate and the grain loss rate (r = –0.86), implying that the 4.2 kg/s feeding rate facilitates a reduction in grain loss during operation within this system. Based on these findings, Scheme 4 was identified as the optimal parameter combination: with a feeding rate of 4.2 kg/s and the installation of auxiliary blades, the average impurity ratio was 49.7%, the distribution uniformity *CV* was 43.6%, and the grain loss rate was minimized to 3.7%.

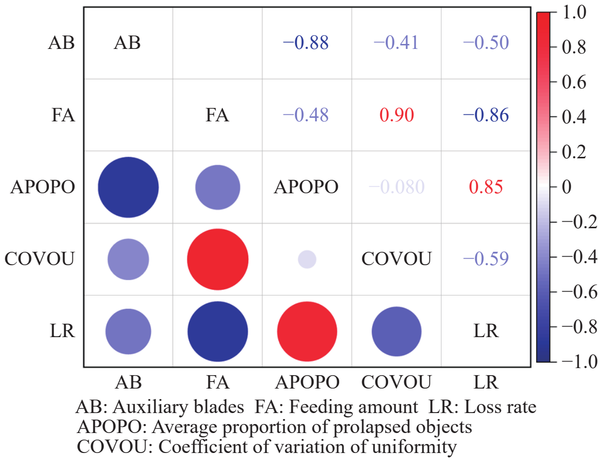

Figure 13 Correlation analysis between parameters and evaluation indicators under different configurations

4 Conclusions

To address the challenges of limited space and power distribution in rapeseed combine harvesters, an innovative pneumatic-assisted threshing and separation device was developed. The device utilizes the rotational kinetic energy of the threshing drum to drive auxiliary blades, generating a directional airflow field that actively reconstructs the suspension paths and motion trajectories of grains and impurities at the source without an external power source. The main conclusions are as follows:

(1) Mechanism and Modeling: Based on kinematics and impact mechanics, a pod-tooth collision model and a critical grain penetration model were established. The feasibility of the design was verified through bench tests of material aerodynamic properties and CFD simulations of the internal airflow field.

(2) Correlation Analysis: Statistical results indicated that the installation of auxiliary blades significantly reduces the impurity ratio in the threshed material (correlation coefficient r = –0.88). Furthermore, increasing the feeding rate within the tested range proved conducive to improving distribution uniformity (r = 0.90) and effectively reducing the grain loss rate (r = –0.86).

(3) Optimization and Performance: Scheme 4 (feeding rate of 4.2 kg/s with auxiliary blades) was identified as the optimal parameter combination. Under these conditions, the average impurity ratio decreased to 49.7%, the coefficient of variation (*CV*) for distribution uniformity was 43.6%, and the grain loss rate was 3.7%, representing a reduction of 2.6 percentage points compared to the non-optimized state.

(4) Component Distribution: At the optimal working condition, the threshed material consisted of 50.3% grains, 35.6% pods, 10.5% stalks, and 3.6% miscellaneous. The study demonstrates that the synergy between a proper feeding rate and pneumatic-assisted technology can significantly optimize separation performance and enhance harvesting quality.

Future research will focus on the refined optimization of the structural parameters and spatial layout of the auxiliary blades to further improve the comprehensive performance of rapeseed combine harvesters.

Acknowledgements

This study was supported by the National Key Research and Development Program of China (Project No. 2023YFD2001000), the National Rapeseed Modern Industrial Technology System of the Ministry of Agriculture and Rural Affairs (Project No. CARS-12), and the Key Area Project of the Jiangsu "333 Talent Program". We sincerely express our gratitude for the support.

[References]

[1] Kerlikowsky F, Krvger K, Hahn A, Schuchardt J P. Multi-micronutrient and omega-3 fatty acid supplementation reduces low-grade inflammation in older participants: an exploratory study. Nutrition Research, 2025. doi: 10.1016/j.nutres.2025.06.005

[2] Swanson D, Block R, Mousa S A. Omega-3 fatty acids EPA and DHA: health benefits throughout life. Advances in Nutrition, 2012; 3(1): 1–7.

[3] Grahovac N, Aleksić M, Trajkovska B, Marjanović J A, Nakov G. Extraction and valorization of oilseed cakes for value-added food components—A review for a sustainable foodstuff production in a case process approach. Foods, 2025; 14(13). doi: 10.3390/foods14132244

[4] Liang Z, Wada M E. Development of cleaning systems for combine harvesters: A review. Biosystems Engineering, 2023; 236: 79–102.

[5] Liu W R, Zhou Y, Xu H M, Fu J W, Zhang N, Xie G, Zhang G Z. Optimization and experiments of the drum longitudinal axial threshing cylinder with rod tooth for rice. Transactions of the CSAE, 2023; 39(15): 34–45. (in Chinese)

[6] Liang Z W, Xu L Z, Baerdemaeker J D, Li Y M, Saeys W. Optimisation of a multi-duct cleaning device for rice combine harvesters utilising CFD and experiments. Biosystems Engineering, 2020; 190: 25–40.

[7] Dong K J, Esfandiary A H, Yu A B. Discrete particle simulation of particle flow and separation on a vibrating screen: Effect of aperture shape. Powder Technology, 2017; 314: 195–202.

[8] Fu J, Chen Z, Han L J, Ren L Q. Review of grain threshing theory and technology. Int J Agric & Biol Eng, 2018; 11(3): 12–20.

[9] Yuan J B, Wang J F, Li H, Qi X D, Wang Y J, Li C. Optimization of the cylindrical sieves for separating threshed rice mixture using EDEM. Int J Agric & Biol Eng, 2022; 15(2): 236–247.

[10] Ma Z, Li Y M, Xu L Z, Chen J, Zhao Z, Tang Z. Dispersion and migration of agricultural particles in a variable-amplitude screen box based on the discrete element method. Computers and Electronics in Agriculture, 2017; 142: 173–180.

[11] Dai F, Song X F, Shi R J, Zhao W Y, Guo W J, Zhang Y. Migration law of flax threshing materials in double channel air-and-screen separating cleaner. Int J Agric & Biol Eng, 2021; 14(3): 81–90.

[12] Dai F, Song X F, Shi R J, Guo W J, Zhao Y M, Wang F, et al. Movement law of the threshing material in threshing and cleaning machine for plot-bred wheat. Int J Agric & Biol Eng, 2022; 15(3): 100–106.

[13] Badretdinov I, Mudarisov S, Lukmanov R, Permyakov V, Ibragimov R, Nasyrov R. Mathematical modeling and research of the work of the grain combine harvester cleaning system. Computers and Electronics in Agriculture, 2019; 165: 104966.

[14] Su Z, Li Y M, Dong Y H, Tang Z, Liang Z W. Simulation of rice threshing performance with concentric and non-concentric threshing gaps. Biosystems Engineering, 2020; 197: 270–284.

[15] Li Y B, Fan H F, Xu Y, Cui T, Su Y, Qiao M M, et al. CFD-DEM investigation of particle dispersion degree on a novel vibrating screen. Powder Technology, 2022; 404: 117497.

[16] Fu J, Zhang J L, Liu F S. Enhanced sieving mechanism of novel cleaning screen and investigation of particle movement characteristics on the screen. Powder Technology, 2024; 431: 119043.

[17] Jin M Z, Zhao Z, Wang Z Q, Xue Z. Attitude angle control method of a vibration screen based on the prediction of material distribution on screen surface. Computers and Electronics in Agriculture, 2025; 233: 110220.

[18] Wu J, Tang Q, Mu S L, Jiang L, Hu Z C. Test and optimization of oilseed rape (*Brassica napus* L.) threshing device based on DEM. Agriculture, 2022; 12(10): 1580.

[19] Xu Q, Cheng X, Chen X. Models for predicting frictional properties of rapeseed. International Agrophysics, 2019; 33(1): 61–66.

[20] Yuan L H, He X, Zhu C H, Wang W Z, Wang M L, Wu S J. Design and test of tangential and longitudinal-axial threshing and separating unit for wheat. Results in Engineering, 2024; 21.

[21] Fu Q K, Fu J, Chen Z, Zhao R Q, Ren L Q. Design and experimental study

of a spiral auxiliary feeding device for lodged corn on a combine harvester. Journal of the ASABE, 2022; 65(1): 31–38.

[22] Minglani D, Sharma A, Pandey H, Dayal R, Joshi J B, Subramaniam S. A review of granular flow in screw feeders and conveyors. Powder Technology, 2020; 366: 369–381.

[23] Kalay E, Boğoçlu M E, Bolat B. Mass flow rate prediction of screw conveyor using artificial neural network method. Powder Technology, 2022; 408: 117757.

[24] El-emam M A, Zhou L, Shi W, Han C, Bai L, Agarwal R. Theories and applications of CFD–DEM coupling approach for granular flow: A review. Archives of Computational Methods in Engineering, 2021; 28(7): 4979–5020.

[25] Cao X L, Li Z H, Li H W, Wang X C, Ma X. Measurement and calibration of the parameters for discrete element method modeling of rapeseed. Processes, 2021; 9(4). doi: 10.3390/pr9040605

[26] Liu Y, Zhou X D, You Z P, Ma B, Gong F Y. Determining aggregate grain size using discrete-element models of sieve analysis. International Journal of Geomechanics, 2019; 19(4): 1376.

[27] Chen M D, Liu X T, Hu P X, Zhai X T, Han Z L, Shi Y L, et al. Study on rotor vibration potato-soil separation device for potato harvester using DEM-MBD coupling simulation. Computers and Electronics in Agriculture, 2024; 218: 108638.

[28] Dai F, Guo W J, Song X F, Shi R J, Qu J F, Zhao W Y. Measurement and simulation of the suspension velocity of flax threshing material using CFD-DEM. Int J Agric & Biol Eng, 2021; 14(5): 230–237.

[29] Jiang T, Guan Z H, Li H T, Zhang M, Mu S L, Wu C Y, et al. Collaborative optimization method of cleaning operational performance and multiparameter online control system for combine harvesters. Computers and Electronics in Agriculture, 2025; 235: 110389.